Astronomy & Astrophysics manuscript no. output
September 20, 2018

Letter to the Editor

TESS's first planet:

a super-Earth transiting the naked-eye star π Mensae

D. Gandolfi[1], O. Barragán[1], J. H. Livingston[2], M. Fridlund[3,4], A. B. Justesen[5], S. Redfield[6], L. Fossati[7], S. Mathur[8,9], S. Grziwa[10], J. Cabrera[11], R. A. García[12,13], C. M. Persson[3], V. Van Eylen[14], A. P. Hatzes[15], D. Hidalgo[8,9], S. Albrecht[5], L. Bugnet[12,13], W. D. Cochran[16], Sz. Csizmadia[11], H. Deeg.[8,9], Ph. Eigmuller[11], M. Endl[16], A. Erikson[11], M. Esposito[15], E. Guenther[15], J. Korth[10], R. Luque[8,9], P. Montañes Rodríguez[8,9], D. Nespral[8,9], P. Niraula[6], G. Nowak[8,9], M. Patzold[10], J. Prieto-Arranz[8,9]

(Affiliations can be found after the references)

Received September 19, 2018; accepted September 20, 2018

ABSTRACT

We report on the confirmation and mass determination of π Men c, the first transiting planet discovered by NASA's *TESS* space mission. π Men is a naked-eye (V=5.65 mag), quiet G0 V star that was previously known to host a sub-stellar companion (π Men b) on a long-period ($P_{\rm orb}$ = 2091 days), eccentric (e = 0.64) orbit. Using *TESS* time-series photometry, combined with *Gaia* data, published UCLES@AAT Doppler measurements, and archival HARPS@ESO-3.6m radial velocities, we find that π Men c is an inner planet with an orbital period of $P_{\rm orb} = 6.25$ days, a mass of $4.51 \pm 0.81\ M_{\oplus}$, and a radius of $1.838^{+0.053}_{-0.052}\ R_{\oplus}$. Based on the planet's orbital period and size, π Men c is a super-Earth located at, or close to, the radius gap, while its mass and bulk density suggest it may have held on to a significant atmosphere. Because of the brightness of the host star, this system is highly suitable for a wide range of further studies to characterize the planetary atmosphere and dynamical properties. We also performed a seismic analysis of the *TESS* light curve and found a hint of an excess power at ∼2600 μHz with individual peaks spaced by ∼120 μHz. Though the signal-to-noise ratio is very low, this is consistent with the predicted frequency of oscillations for a star of this type, hinting at the asteroseismic potential of the *TESS* mission.

Key words. Planetary systems – Planets and satellites: individual: π Mensae b, π Mensae c, π Mensae,-- Stars: fundamental parameters – Stars: individual: π Mensae – Techniques: photometric – Techniques: radial velocities

1. Introduction

Successfully launched on 18 April 2018, NASA's Transiting Exoplanet Survey Satellite (*TESS*; Ricker et al. 2015) will provide us with a leap forward in understanding the diversity of small planets ($R_p < 4\,R_{\oplus}$). Unlike previous space missions, *TESS* is performing an all-sky transit survey focusing on bright stars ($5 < V < 11$ mag), so that detailed characterizations of the planets and their atmospheres can be performed. In its two-year prime mission, *TESS* observes first the southern and then the northern ecliptic hemisphere. The survey is broken up into 26 anti-solar sky sectors. *TESS* uses 4 cameras to observe each sector, resulting in a combined field of view of $24° \times 96°$, and increasing overlap between sectors towards the ecliptic poles provides greater sensitivity to smaller and longer-period planets in those regions of the celestial sphere. *TESS* records full-frame images of its entire field of view every 30 minutes and observes ∼200 000 preselected main-sequence stars with a cadence of ∼2 minutes. The mission will certainly open a new era in the studies of close-in small planets, providing us with cornerstone objects amenable to both mass determination – via Doppler spectroscopy – and atmospheric characterization – via transmission spectroscopy with NASA's James Webb space telescope (*JWST*) and the next generation of extremely large ground-based telescopes (*ELT*, *TMT*, and *GMT*).

Following a successful commissioning of 3 months, *TESS* started the science operation on 25 July 2018 by photometrically monitoring its first sector (Sector 1), which is centered at coordinates $\alpha = 352.68°$, $\delta = -64.85°$ (J2000). Shortly after ∼30 days of (almost) continuous observations in Sector 1, 73 transiting planet candidates were detected in the 2-min cadence light curves by the *TESS* team and made available to the scientific community through a dedicated web portal hosted at the Massachusetts Institute of Technology (MIT) web page[1].

In this letter, we present the spectroscopic confirmation of π Men c, the first transiting planet discovered by the *TESS* space mission. The host star is π Mensae (HD 39091; Table 1), a naked-eye (V=5.65 mag), relatively inactive ($\log R'_{\rm HK} = -4.941$; Gray et al. 2006), G0 V star already known to host a sub-stellar companion (π Men b) on a ∼2100-day eccentric ($e \approx 0.6$) orbit (Jones et al. 2002). π Men c is a $1.84\,R_{\oplus}$ planet with an orbital period of 6.27 days. Using *Gaia* photometry, archival HARPS Doppler data, and published UCLES high-precision radial velocities (RVs) we confirmed the planetary nature of the transiting signal detected by *TESS* and derived the planet's mass [2].

[1] Available at https://tess.mit.edu/alerts/.
[2] During the preparation of this manuscript, an independent investigation of this system was publicly announced (Huang et al. 2018).

Table 1. Main identifiers, coordinates, parallax, optical, and infrared magnitudes of π Men

Parameter	Value	Source
HD	39091	
TIC ID	261136679	TIC
TOI ID	144	*TESS* Alerts
Gaia DR2 ID	4623036865373793408	*Gaia* DR2
RA (J2000)	05 37 09.885	*Gaia* DR2
RA (J2000)	-80 28 08.831	*Gaia* DR2
π	54.705 ± 0.0671 mas	*Gaia* DR2
V	5.65 ± 0.01	Mermilliod (1987)
B	6.25 ± 0.01	Mermilliod (1987)
J	4.869 ± 0.272	2MASS
H	4.424 ± 0.226	2MASS
K_s	4.241 ± 0.027	2MASS
G	5.4907 ± 0.0014	*Gaia* DR2
G_{BP}	5.8385 ± 0.0041	*Gaia* DR2
G_{RP}	5.0643 ± 0.0034	*Gaia* DR2

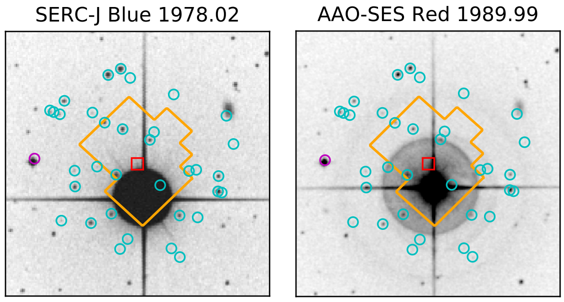

Fig. 1. $5' \times 5'$ archival images with the *TESS* photometric aperture overplotted in orange, the *Gaia* DR2 position (J2015.5) of π Men indicated by a red square, and other *Gaia* DR2 sources within $2'$ of π Men indicated by circles. The magenta circle indicates the position of *Gaia* DR2 4623036143819289344, a nearby source bright enough to be the host of the observed transit signals (see Section 3), and cyan circles indicate sources that are too faint.

2. *TESS* photometry

We downloaded the *TESS* Sector 1 light curves from the MIT website. For the *TESS* object of interest TOI-144 (aka, π Men, HD 39091, TIC 261136679), the light curve is provided by the NASA Ames SPOC center. The time-series includes 18 036 short-cadence ($T_{\mathrm{exp}} = 2$ min) photometric measurements. *TESS* observations started on 25 July 2018 and ended on 22 August 2018. We removed any measurements that have a non-zero “Quality” flag, i.e., those suffering from cosmic rays or instrumental issues. We removed any long term stellar variability by fitting a cubic spline with a width of 0.75 days. We searched the light curve for transit signals using the Box-least-squares algorithm (BLS; Kovács et al. 2002). We detected the signal of π Men c with a signal-to-noise ratio (S/N) of 9.1 and our ephemeris is consistent with that reported by the *TESS* team. We did not find any additional transit signal with (S/N) > 6. We also performed a periodogram and auto-cross-correlation analysis in the attempt to extract the rotation period of the star from the out-of-transit *TESS* light curve, but we found no significant rotation signal in the light curve.

3. Limits on photometric contamination

As a result of the $\sim 21''$ pixel scale of the *TESS* detectors, photometric contamination due to chance alignment with a background source is more likely than in previous transit surveys, such as *Kepler*. We investigated this possibility using archival images of π Men from the SERC-J and AAO-SES surveys[3] and *Gaia* DR2 (Gaia Collaboration et al. 2018). The *TESS* photometric aperture used to create the SPOC light curve is approximately 6×6 *TESS* pixels in extent, so we executed a query of *Gaia* DR2 centered on the coordinates of π Men from the *TESS* Input Catalog (TIC), using a search radius of $2'$. The archival images were taken in 1978 and 1989, so π Men appears significantly offset from its current position due to proper motion; no background source is visible near the current position of π Men. Figure 1 shows *Gaia* DR2 source positions overplotted on the archival images, along with the *TESS* photometric aperture.

Assuming a maximum eclipse depth of 100%, the measured transit depth (see Section 8) puts an upper limit on the magnitude of a putative eclipsing binary within the photometric aperture, since a fainter source would be diluted too much by the flux from π Men. As the *Gaia* G_{RP} band-pass is a good approximation to the *TESS* band-pass, we find a limiting magnitude of $G_{\mathrm{RP,max}}$ = 14.1 mag. Assuming an aperture radius of $60''$ ($120''$), a simulated stellar population along the line of sight to π Men from `TRILEGAL`[4] (Girardi et al. 2005) implies a frequency of 0.3578 (1.4312) stars brighter than $G_{\mathrm{RP,max}}$. Indeed, only one other *Gaia* DR2 source within $2'$ of π Men is brighter than $G_{\mathrm{RP,max}}$, consistent with the expectation from `TRILEGAL`: *Gaia* DR2 4623036143819289344 ($G_{\mathrm{RP}} = 12.1644 \pm 0.0011$ mag, separation $\approx 118''$). As this source is clearly outside of the *TESS* photometric aperture, we conclude that π Men is the true host of the transit signal as seen by *TESS*, and that photometric dilution from sources fainter than $G_{\mathrm{RP,max}}$ is negligible.

4. UCLES and HARPS archival spectra

Jones et al. (2002) reported on the detection of a long-period ($P_{\mathrm{orb}} \approx 2100$ days), eccentric ($e \approx 0.6$), sub-stellar companion to π Men with a minimum mass of $M_{\mathrm{b}} = 10.3\ M_{\mathrm{Jup}}$. Their discovery is based on 28 RV measurements obtained between November 1998 and April 2002 using the UCLES spectrograph mounted at the 3.92-m Anglo-Australian Telescope at Siding Spring Observatory. Fourteen additional UCLES RVs were published by Butler et al. (2006). For the sake of clarity, we list the 42 UCLES RVs in Table 3.

We also retrieved from the ESO public archive 145 high-resolution ($R \approx 115\,000$) spectra of π Men, taken with the HARPS spectrograph (Mayor et al. 2003) mounted at the ESO-3.6m telescope of La Silla observatory (Chile). The observations were carried out between 28 December 2012 and 17 March 2017 UTC, as part of the observing programs 072.C-0488, 183.C-0972, and 192.C-0852. The retrieved data-set includes Echelle and order-merged spectra in flexible image transport system (FITS) format, along with additional FITS files containing the cross-correlation function (CCF) and its bisector, computed from the HARPS pipeline using a G2 numerical mask. We extracted from the FITS headers the barycentric Julian dates, the RVs and their uncertainties, along with the full-with half maximum (FWHM) and bisector span (BIS) of the CCF, and the signal-to-noise ratio per pixel at 5500 Å. On June 2015, the HARPS fibre

[3] Available at `http://archive.stsci.edu/cgi-bin/dss_form`.

[4] Available at `http://stev.oapd.inaf.it/cgi-bin/trilegal`.

bundle was upgraded (Lo Curto et al. 2015). To account for the RV offset caused by the instrument refurbishment, we treated the HARPS RVs taken before/after June 2015 as two different data-sets (Table 4 and 5). Following Eastman et al. (2010), we converted the heliocentric Julian dates ($\mathrm{HJD}_{\mathrm{UTC}}$) of the UCLES time stamps and the barycentric Julian ($\mathrm{BJD}_{\mathrm{UTC}}$) of the HARPS time stamps into barycentric Julian dates in barycentric dynamical time ($\mathrm{BJD}_{\mathrm{TDB}}$).

5. Stellar fundamental parameters

We determined the spectroscopic parameters of π Men from the co-added HARPS spectrum, which has a S/N per pixel of ~1880 at 5500 Å. We used Spectroscopy Made Easy (`SME`; Valenti & Piskunov 1996; Valenti & Fischer 2005; Piskunov & Valenti 2017), a spectral analysis tool that calculates synthetic spectra and fits them to high-resolution observed spectra using a χ^2 minimizing procedure. The analysis was performed with the non-LTE `SME` version 5.2.2, along with `ATLAS 12` one-dimensional model atmospheres (Kurucz 2013).

In order to determine the micro-turbulent (v_{mic}) and macro-turbulent (v_{mac}) velocities, we used the empirical calibration equations for Sun-like stars from Bruntt et al. (2010) and Doyle et al. (2014), respectively. The effective temperature T_{eff} was measured fitting the wings of the H_α line (Fuhrmann et al. 1993; Axer et al. 1994; Fuhrmann et al. 1994, 1997b,a). We excluded the core of H_α because of its origin in higher layers of stellar photospheres. The surface gravity $\log g_\star$ was determined from the wings of the Ca I λ 6102, λ 6122, λ 6162 Å triplet, and the Ca I λ 6439 Å line. We measured the iron abundance [Fe/H] and projected rotational velocity $v \sin i_\star$ by simultaneously fitting the unblended iron lines in the spectral region 5880–6600 Å.

We found an effective temperature of T_{eff} = 5870 ± 50 K, surface gravity $\log g_\star = 4.33 \pm 0.09$ (cgs), and an iron abundance relative to solar of [Fe/H] = 0.05 ± 0.09 dex. We measured a [Ca/H] abundance of 0.07 ± 0.10 dex. The projected rotational velocity was found to be $v \sin i_\star = 3.3 \pm 0.5$ km s^{-1}, with $v_{\mathrm{mic}} = 1.06 \pm 0.10$ km s^{-1} and $v_{\mathrm{mac}} = 3.35 \pm 0.4$ km s^{-1}. These values were confirmed by modeling the Na I doublet at 5889.95 and 5895.924 Å. We detected no interstellar sodium, as expected given the vicinity of the star (d=18.3 pc).

We used the BAyesian STellar Algorithm (`BASTA`, Silva Aguirre et al. 2015) with a large grid of `GARSTEC` stellar models (Weiss & Schlattl 2008) to derive the fundamental parameters of π Men. We built the spectral energy distribution (SED) of the star using the magnitudes listed in Table 1, and then fitted the SED along with our spectroscopic parameters (T_{eff}, $\log g_\star$, [Fe/H]) and *Gaia* parallax to a grid of `GARSTEC` models. Following Luri et al. (2018), we quadratically added 0.1 mas to the nominal uncertainty of *Gaia* parallax to account for systematic uncertainties of *Gaia* astrometry. We adopted a minimum uncertainty of 0.01 mags for the *Gaia* magnitudes to account for systematic uncertainties in the *Gaia* photometry. Given the proximity of the star (d=18.3 pc), we assumed no interstellar reddening.

We found that π Men has a mass of $M_\star = 1.02 \pm 0.03\ M_\odot$ and a radius of $R_\star = 1.10 \pm 0.01\ R_\odot$, implying a surface gravity of $\log g_\star = 4.36 \pm 0.02$ (cgs), in agreement with the spectroscopically derived value of 4.33 ± 0.09. The stellar models constrain the age of the star to be 5.2 ± 1.1 Gyr. The fundamental parameters of π Men are given in Table 2. We note that the uncertainties on the derived parameters are internal to the stellar models used and do not include systematic uncertainties related to input physics or the bolometric correction.

6. Seismic analysis

We also performed a seismic analysis of the *TESS* light curve to look for oscillations in order to better characterize the stellar parameters. Our light curve correction consists of three steps. First, we corrected the PDCSAP flux performing a robust locally weighted regression as described in Cleveland (1979) in order to smooth long period variation from the light curve without removing any transit signal. We also calibrated the data following the methods described in García et al. (2011). The results of both analyses provided similar seismic results, although the corrections applied were very different. As a second step we removed the transits by folding the light curve at the period of the planet transit and filtering it with a wavelet transform using an "à trous" algorithm (Starck & Murtagh 2002, 2006). Finally as the last step, the gaps of the resultant light curve were interpolated using inpainting techniques following Pires et al. (2015) and García et al. (2014).

First we used the FliPer metric (Bugnet et al. 2018) to estimate $\log g_\star$ directly from the global power of the power spectrum density. Unfortunately, due to the filters applied to the light curve to flatten it and properly remove the transits, part of the power below ~100 μHz is removed providing only a lower limit of the value of surface gravity or the frequency of maximum power of the modes. Therefore, we applied the standard seismic A2Z pipeline (Mathur et al. 2010) to look for the power excess due to acoustic modes. While the blind search did not provide any detection, we then estimated where we would expect the acoustic modes given the spectroscopic parameters derived in this paper. The modes are expected around 2500 μHz. The power spectrum of the star shows a slight excess of power around 2600 μHz (frequency of maximum power or ν_{max}) and the A2Z pipeline that computes the power spectrum of the power spectrum detects a signal at $119.98 \pm 9.25\ \mu$Hz, which is the large frequency separation ($\Delta\nu$ is the frequency difference between 2 modes of same degree and consecutive orders). This value corresponds to the $\Delta\nu$ expected for modes at $2607 \pm 16\ \mu$Hz. It is very unlikely that noise would have such a pattern in such a region of the power spectrum. Using $\Delta\nu$, $\nu_{\max}$, and T_{eff}, along with the solar scaling relations from Kjeldsen & Bedding (1995), we found a stellar mass of $M_\star = 1.02 \pm 0.15\ M_\odot$ and a stellar radius of $R_\star = 1.09 \pm 0.10\ R_\odot$, in agreement with the spectroscopic values (Sect. 5). We note that, given the large uncertainties on $\nu_{\max}$ and $\Delta\nu$, the stellar mass and radius determined from the solar scaling relations have large uncertainties, as expected given the predicted detectability of solar-like oscillations with *TESS* (Campante 2017).

7. Frequency analysis of the Doppler data

We performed a frequency analysis of the UCLES and HARPS RVs in order to search for the presence of the transiting planet in the Doppler data, and look for possible additional periodic signals. The generalized Lomb-Scargle (GLS; Zechmeister & Kürster 2009) periodogram of the combined UCLES and HARPS RVs[5] shows a very significant peak at the orbital frequency of the outer sub-stellar companion ($f_b = 0.0005$ c/d), with a false-alarm probability (FAP) lower than 10^{-10}.

The upper panel of Fig. 2 displays the GLS periodogram of the RV residuals following the subtraction of the Doppler signal induced by the outer sub-stellar object. We found a significant

[5] We accounted for the instrumental offsets using the values derived in Sect. 8.

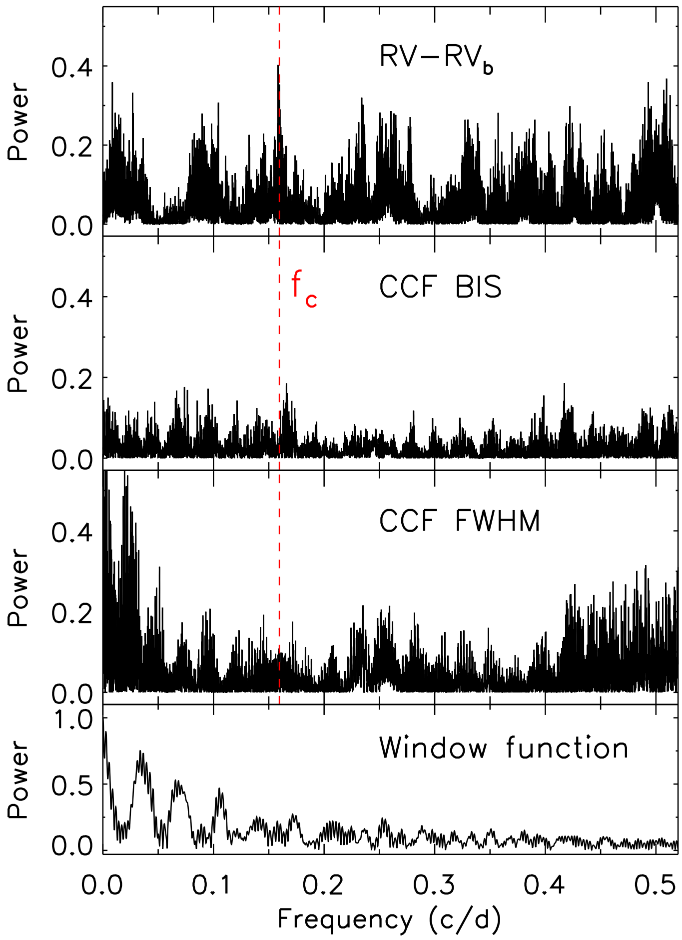

Fig. 2. *First panel*: GLS periodogram of the UCLAS and HARPS RV residuals following the subtraction of the Doppler reflex motion induced by the outer sub-stellar companion. *Second and third panels*: GLS periodogram of the BIS and FWHM of the HARPS CCF (data acquired with the old fibre bundle). *Fourth panel*: periodogram of the window function of the combined RV measurements. The dashed vertical red line marks the orbital frequency of the transiting planet ($f_c = 0.16$ c/d).

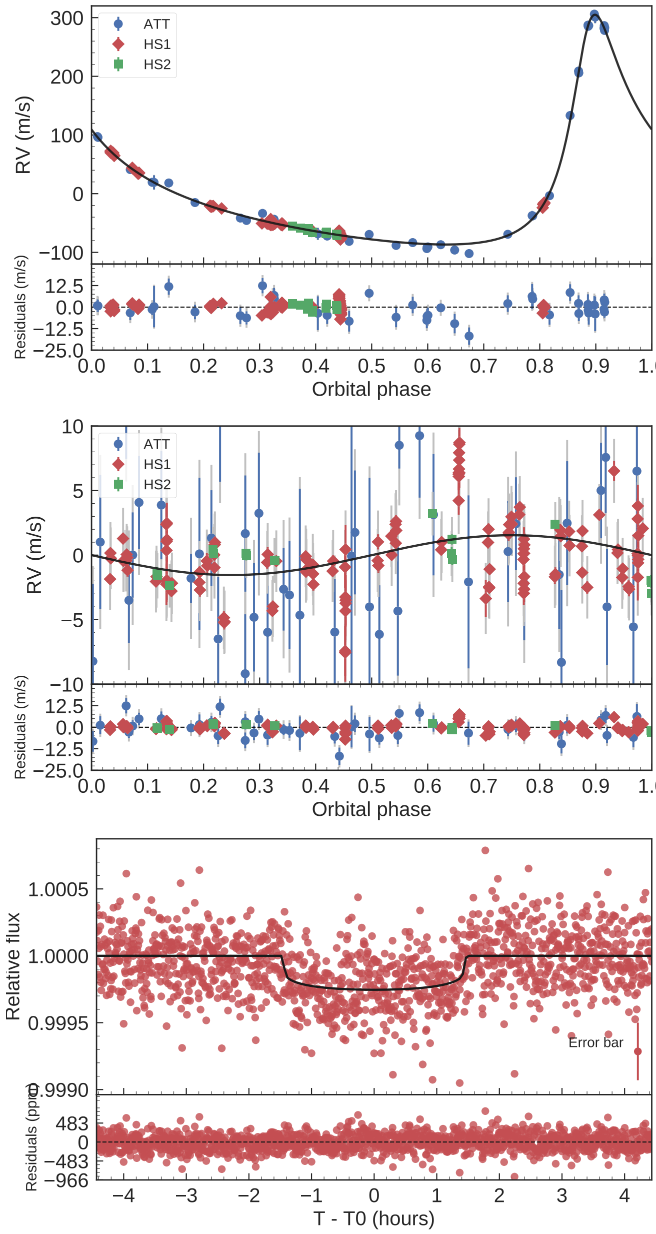

Fig. 3. Phase-folded RV curves of π Men b (upper panel) and c (middle panel), and transit light curve of π Men c (lower panel). The best fitting transit and Keplerian models are overplotted with thick black lines. The *TESS* data points are shown with red circles (lower panel). The ATT data and the two sets of HARPS RVs (HS1 and HS2) are shown with circles, diamonds, and squares, respectively.

peak (FAP $< 10^{-5}$) at the frequency of the transit signal detected by *TESS* ($f_c = 0.16$ c/d), with a semi-amplitude RV variation of $\sim$1.5 m s^{-1}. The peak has no counterparts in the periodograms of the HARPS activity indicators (second and third panels of Fig. 2), suggesting that the signal is induced by the presence of an orbiting planet with a period of 6.3 days. We note that, based merely on the RV data-set, we would have been able to detect the presence of π Men c even in the absence of the *TESS* transit signal.

We also subtracted the Doppler reflex motion induced by the transiting planet from our RV data and searched the residuals for additional periodic signal but found no peak with FAP $< 10^{-4}$.

8. Joint analysis of the transit and Doppler data

We performed a joint analysis of the photometric and RV time-series using the software suite `pyaneti` (Barragán et al. 2018). `pyaneti` allows for parameter estimation from posterior distributions calculated using Markov chain Monte Carlo methods.

We extracted 10 hours of *TESS* data points centered around each of the 5 transits observed by *TESS*. The 5 segments were de-trended using the code `exotrending` (Barragán & Gandolfi 2017), fitting a second-order polynomial to the out-of-transit data. We used all 187 Doppler measurements presented in Sect. 4 and accounted for the RV offsets between the different instruments and the two HARPS setups.

The RV model consists of two Keplerians to account for the Doppler signal induced by planets *b* and *c*. We fitted for a RV jitter term for each instrument/setup to account for instrumental noise not included in the nominal uncertainties, and/or to account for any stellar activity-induced RV variation. We modeled the *TESS* transit light curves using the limb-darkened quadratic model of Mandel & Agol (2002). For the limb darkening coefficients, we set Gaussian priors using the values derived by Claret (2017) for the *TESS* pass-band. We imposed conservative error bars of 0.1 on both the linear and the quadratic limb-darkening term. A preliminary analysis showed that the transit light curve poorly constrains the scaled semi-major axis ($a/R_\star$). We therefore set a Gaussian prior on $a/R_\star$ using Kepler's third's law, the orbital period, and the derived stellar parameters (Sect. 5). Because the eccentricity of planet *c* is poorly constrained by the observations, we fixed it to zero for our analysis (see also Section 9). We imposed uniform priors for the remaining fitted parameters. Details about the fitted parameters and prior ranges are given in Table 2. Before performing the final analysis, we ran a numerical experiment to check if the *TESS* 2 min integration time needs to be taken into account following Kipping (2010). We found no differences in the posterior distributions for fits with and without re-sampling; we thus proceeded with our analysis without re-sampling. We used 500 independent Markov chains initialized randomly inside the prior ranges. Once all chains converged, we used the last 5 000 iterations and saved the chains states every 10 iterations. This approach generates a posterior distribution of 250 000 points for each fitted parameter. Table 2 lists the inferred planetary parameters. They are defined as the median and 68% region of the credible interval of the posterior distributions for each fitted parameter. The transit and RV curves are shown in Fig. 3.

9. Discussion and conclusion

π Men is a bright (V=5.65 mag) Sun-like star (SpT=G0 V) known to host a sub-stellar companion (π Men b) on a long-period eccentric orbit (Jones et al. 2002). Combining *Gaia* photometry with archival RV measurements we confirmed that the P=6.27 day transit signal detected in the *TESS* light curve of π Men is caused by a *bona-fide* transiting sub-Earth and derived its mass. π Men c becomes *TESS*'s first confirmed planet.

π Men joins the growing number of stars known to host both long-period Jupiter analogues and close-in small planets ($R_\mathrm{p} < 4\,R_\oplus$). Bryan et al. (2018) recently found that the occurrence rate of companions between 0.5–20 M_Jup at 1–20 AU in systems known to host inner small planets is $39 \pm 7\%$, suggesting that the presence of outer gas giant planets does not prevent the formation of inner Earth- and Neptune-size planets. We performed a dynamical stability analysis of π Men using the software `mercury6` (Chambers 1999). Assuming co-planar orbits, we let the system evolve for 100 000 yr. For π Men b we found negligible changes of the semi-major axis and eccentricity of $< 2.6 \times 10^{-3}$ AU and 3×10^{-4}, respectively. For π Men c we found no variation larger than 1×10^{-5} of its semi-major axis, with changes of its eccentricity $\lesssim$0.05.

The actual orientation of the outer planet's orbit is unknown. While we know the inner planet's inclination, because it transits, its eccentricity is poorly constrained by the data. Compact multi-planet systems have been observed to have near-zero eccentricities (e.g. Hadden & Lithwick 2014; Van Eylen & Albrecht 2015; Xie et al. 2016). However, planets with only a single transiting planet appear to often be "dynamically hotter", and many have a non-zero eccentricity, which can, e.g., be described by the positive half of a zero-mean Gaussian distribution, with a dispersion $\sigma_e = 0.32 \pm 0.06$ (Van Eylen et al. 2018b). The outer planet, π Men c, has an orbital eccentricity of ~0.64. A far-out giant planet, such as planet *c*, may in fact increase the orbital eccentricity of a close-in super-Earth, such as planet *b* (see, e.g., Mustill et al. 2017; Hansen 2017; Huang et al. 2017). Following Van Eylen et al. (2018b), we found an orbital eccentricity based on the transit data alone of [0, 0.45] at 68% confidence. Because the current RV observations cannot constrain the eccentricity either, we fixed it to zero in the above analysis (see Section 8). The brightness of the host star makes this planetary system an exciting target for further RV follow-up to measure the inner planet's eccentricity.

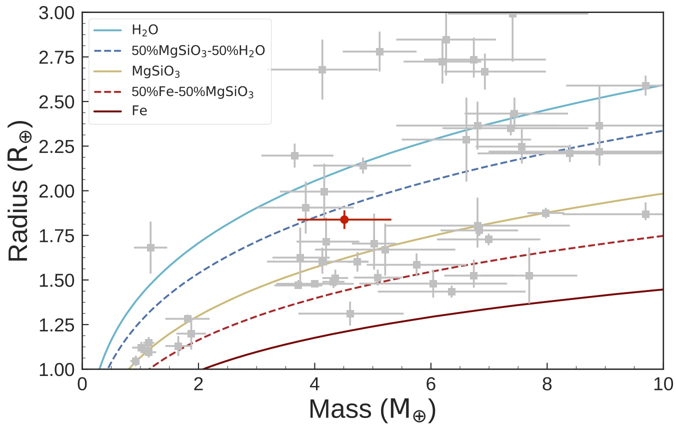

Fig. 4. Mass-radius for low mass ($M_\mathrm{p} < 10\ M_\oplus$) small ($R_\mathrm{p} < 3\,M_\oplus$) planets with mass-radius measurements better than 25% (from `http://www.astro.keele.ac.uk/jkt/tepcat/`; Southworth et al. 2007). Composition models from Zeng et al. (2016) are displayed with different lines and colors. The solid red circle marks the position of π Men c.

The transiting planet π Men c has a mass of $M_\mathrm{c} = 4.51 \pm 0.81\ M_\oplus$ and a radius of $R_\mathrm{c} = 1.838^{+0.053}_{-0.052}\ R_\oplus$, yielding a mean density of ρ_c=$3.99^{+0.81}_{-0.77}$ g cm^{-3}. Figure 4 shows the mass-radius diagram for small planets whose masses have been determined with a precision better than 25 %. Theoretical models from Zeng et al. (2016) are overplotted using different lines and colors. The position of π Men c suggests a composition of Mg-silicates and water. Alternatively, the planet might have a solid core surrounded by a gas envelope. At short orbital periods, super-Earths and sub-Neptunes are separated by a radius gap at $\approx$1.6 $R_\oplus$ (Fulton et al. 2017; Van Eylen et al. 2018a). The exact location of the radius gap is observed to be a function of the orbital period (Van Eylen et al. 2018a), as predicted by models of photo-evaporation (e.g. Owen & Wu 2013; Lopez & Fortney 2013). Van Eylen et al. (2018a) find that the radius gap is located at $\log R = m \times \log P + a$, where $m = -0.09^{+0.02}_{-0.04}$ and $a = 0.37^{+0.04}_{-0.02}$. At the orbital period of π Men c, i.e. P_orb = 6.27 days, the radius gap is then located at $R_\mathrm{p} = 1.99 \pm 0.20\ R_\oplus$. This suggests that π Men c, with a radius of $R_\mathrm{p} = 1.838^{+0.053}_{-0.052}\ R_\oplus$, is located just around the radius gap, or slightly below, although the measured density suggests that the planet may have held on to (part of) its atmosphere.

The naked-eye brightness of π Men immediately argues that any transiting planet will be attractive for atmospheric characterization. Observations of a planetary atmosphere through transmission spectroscopy during transit provide opportunities to measure the extent, kinematics, abundances, and structure of the atmosphere (Seager & Deming 2010). Such measurements can be utilized to address fundamental questions such as planetary atmospheric escape and interactions with the host star (Cauley et al. 2017), formation and structure of planetary interiors (Owen et al. 1999), planetary and atmospheric evolution (Öberg et al. 2011), and biological processes (Meadows & Seager 2010).

The left panel of Fig. 5 displays a relative atmospheric detection S/N metric normalized to π Men c for all known small exoplanets with $R_p < 3\ R_\oplus$. The sample is taken from the Exoplanet Orbit Database[6] as of September 2018. The atmospheric signal

[6] Available at `exoplanets.org`.

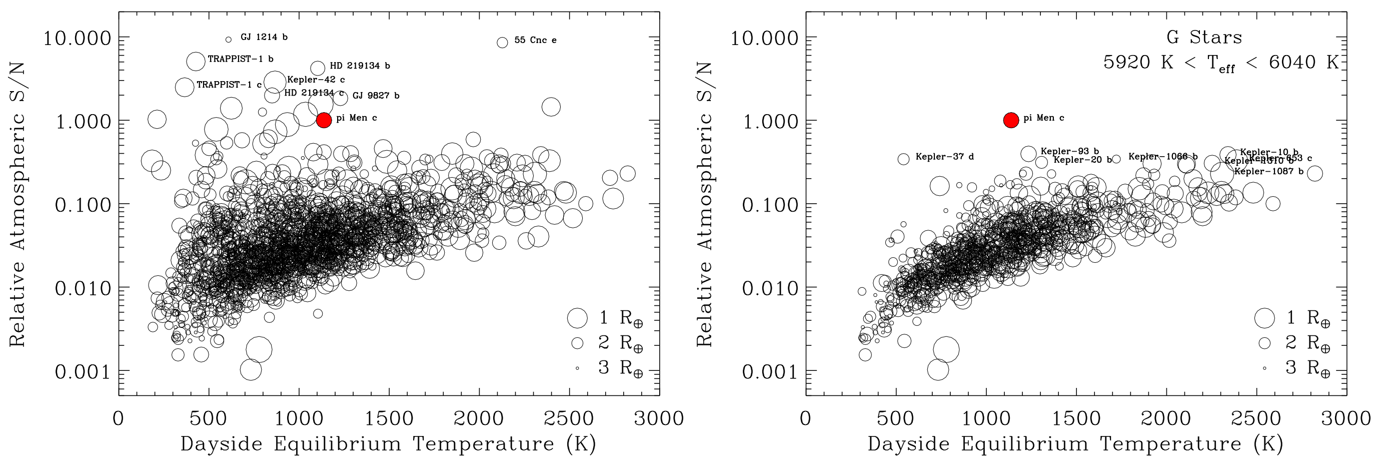

Fig. 5. *Left Panel*: Relative S/N of an atmospheric signal for all exoplanets with $R_\mathrm{p} < 3\,R_\oplus$ as a function of planetary equilibrium temperature. The π Men c planet is used as the atmospheric signal reference and it is indicated by the filled circle. It is among the top 15 most favorable planets for atmospheric characterization. *Right panel*: Same as the left panel, simply limited to solar type host stars (i.e., G-type stars; $5920 < T_\mathrm{eff} < 6040$ K). The π Men c planet is by far the most favorable planet around such a star for atmospheric characterization. The other optimal atmospheric targets all transit K and M stars. For this reason, the coronal and stellar wind properties that interact with the π Men c atmosphere may be distinctly different to those experienced by the rest of the sample.

is calculated in a similar way to Gillon et al. (2016) and Niraula et al. (2017). This calculation assumes similar atmospheric properties (e.g., Bond albedo, mean molecular weight) for all planets. Large atmospheric signals result from hot, extended atmospheres of planets that transit small, cool stars. For this reason, planets transiting such stars as GJ 1214 and TRAPPIST-1 are excellent targets for this kind of study. Yet, the brightness of the host star along with the period and duration of the transit also significantly contribute to the ability to build up a sufficiently high S/N to detect atmospheric signals. We used the J-band flux (e.g., H_2O measurements with *JWST*; Beichman et al. 2014), and weight the metric to optimize the S/N ratio over a period of time rather than per transit.

In the context of all small planets ($R_\mathrm{p} < 3\,R_\oplus$), π Men c has the 15$^{\mathrm{th}}$ strongest atmospheric signal, behind GJ 1214 b, 55 Cnc e, the TRAPPIST-1 planets, the HD 219134 planets, the Kepler-42 planets, GJ 9827 b, and others. Yet, π Men is unique among this notable group of stars in that it is the only G-type star (Fig. 5, right panel). All of the other exoplanets transit K- or M-type stars. The brightness of π Men is able to overcome the disadvantage of a small planet transiting a slightly larger star, to provide the best opportunity of probing the atmospheric properties of a super-Earth orbiting a solar type star. Given the significant changes in the structure of stellar coronae and stellar winds between G- and M-type stars, the atmospheric properties and evolution of π Men c may be distinctly different from the atmospheres detected around the sample around very low mass M-type stars (e.g., GJ 1214 and TRAPPIST-1). For example, the TRAPPIST-1 e, f, and g planets essentially orbit within the stellar corona of the host star and may be subject to a substantial stellar wind, which will result in a strong injection of energy in the atmosphere and may prevent the formation of a significant atmosphere (Cohen et al. 2018). When inferring the properties of coronae and winds of stars other than the Sun, we often have to use poorly constrained models and empirical correlations, the validity of which are best for stars that are quite similar to the Sun. In this respect, π Men is a unique laboratory because of its greater similarities to the Sun with respect to all the other stars known to host mini-Neptunes and Super-Earths amenable to multi-wavelength atmospheric characterization.

We further study the long-term stability of a possible hydrogen-dominated atmosphere by estimating the mass-loss rates. To this end, we employ the interpolation routine described by Kubyshkina et al. (2018), which interpolates the mass-loss rate among those obtained with a large grid of one-dimensional upper atmosphere hydrodynamic models for super-Earths and sub-Neptunes. Employing the values listed in Table 2 and a Sun-like high-energy emission, which is a reasonable assumption given that π Men has a temperature and age similar to those of the Sun, we obtained a mass-loss rate of $4.4\mathrm{x}10^9$ g s$^-$1, which corresponds to 0.5% of the estimated planetary mass per Gyr. This indicates that the question whether the planet still holds a hydrogen-dominated atmosphere or not greatly depends on the initial conditions, namely, how much hydrogen the planet accreted during its formation. If the planet originally accreted a small hydrogen-dominated atmosphere, with a mass of only a few % of the total planetary mass, we can expect it to be for the vast majority lost, particularly taking into account that the star was more active in the past. In contrast, a significant hydrogen mass fraction would still be present if the planet originally accreted a large amount of hydrogen. The inferred bulk density hints at the possible presence of a hydrogen-dominated atmosphere, but it does not give a clear indication. Ultraviolet observations aiming at detecting hydrogen Ly$_\alpha$ absorption and/or carbon and oxygen in the upper planetary atmosphere would be decisive in identifying its true nature.

Acknowledgements. Davide Gandolfi is lovingly grateful to Conny Konnopke for her unique support during the preparation of this paper, and her valuable suggestions and comments. J.H.L. gratefully acknowledges the support of the Japan Society for the Promotion of Science (JSPS) Research Fellowship for Young Scientists. M.F. and C.M.P. gratefully acknowledge the support of the Swedish National Space Board. A.P.H., Sz.Cs., S.G., J.K., M.P., and M.E. acknowledge support by DFG (Deutsche Forschungsgemeinschaft) grants HA 3279/12-1, PA525/18-1, PA525/19-1, PA525/20-1, and RA 714/14-1 within the DFG Schwerpunkt SPP 1992, "Exploring the Diversity of Extrasolar Planets." We are grateful for the use of *TESS* Alert data, currently in a beta test phase, which come from pipelines at the *TESS* Science Office and at the *TESS* Science Processing Operations Center. Funding for the *TESS* mission is provided by NASA's Science Mission directorate. This work has made use of data from the European Space Agency (ESA) mission *Gaia* (`https://www.cosmos.esa.int/gaia`), processed by the *Gaia* Data Processing and Analysis Consortium (DPAC, `https://www.cosmos.esa.int/web/gaia/dpac/consortium`). Funding for the DPAC has been provided by national institutions, in particular the institutions participating in the *Gaia* Multilateral Agreement. We acknowledge the traditional owners of the land on which the AAT stands, the Gamilaraay people, and pay our respects to elders past and present.

References

Axer, M., Fuhrmann, K., & Gehren, T. 1994, A&A, 291, 895
Barragán, O. & Gandolfi, D. 2017, Exotrending: Fast and easy-to-use light curve detrending software for exoplanets, Astrophysics Source Code Library
Barragán, O., Gandolfi, D., & Antoniciello, G. 2018, ArXiv e-prints [arXiv:1809.04609]
Beichman, C., Benneke, B., Knutson, H., et al. 2014, PASP, 126, 1134
Bruntt, H., Bedding, T. R., Quirion, P.-O., et al. 2010, MNRAS, 405, 1907
Bryan, M. L., Knutson, H. A., Fulton, B., et al. 2018, ArXiv e-prints [arXiv:1806.08799]
Bugnet, L., García, R. A., Davies, G. R., et al. 2018, ArXiv e-prints [arXiv:1809.05105]
Butler, R. P., Wright, J. T., Marcy, G. W., et al. 2006, ApJ, 646, 505
Campante, T. L. 2017, in European Physical Journal Web of Conferences, Vol. 160, European Physical Journal Web of Conferences, 01006
Cauley, P. W., Redfield, S., & Jensen, A. G. 2017, AJ, 153, 185
Chambers, J. E. 1999, MNRAS, 304, 793
Claret, A. 2017, A&A, 600, A30
Cleveland, W. S. 1979, Journal of the American Statistical Association, 74, 829
Cohen, O., Glocer, A., Garraffo, C., Drake, J. J., & Bell, J. M. 2018, ApJ, 856, L11
Doyle, A. P., Davies, G. R., Smalley, B., Chaplin, W. J., & Elsworth, Y. 2014, MNRAS, 444, 3592
Eastman, J., Siverd, R., & Gaudi, B. S. 2010, PASP, 122, 935
Fuhrmann, K., Axer, M., & Gehren, T. 1993, A&A, 271, 451
Fuhrmann, K., Axer, M., & Gehren, T. 1994, A&A, 285, 585
Fuhrmann, K., Pfeiffer, M., Frank, C., Reetz, J., & Gehren, T. 1997a, A&A, 323, 909
Fuhrmann, K., Pfeiffer, M. J., & Bernkopf, J. 1997b, A&A, 326, 1081
Fulton, B. J., Petigura, E. A., Howard, A. W., et al. 2017, AJ, 154, 109
Gaia Collaboration, Brown, A. G. A., Vallenari, A., et al. 2018, ArXiv e-prints [arXiv:1804.09365]
García, R. A., Hekker, S., Stello, D., et al. 2011, MNRAS, 414, L6
García, R. A., Mathur, S., Pires, S., et al. 2014, A&A, 568, A10
Gillon, M., Jehin, E., Lederer, S. M., et al. 2016, Nature, 533, 221
Girardi, L., Groenewegen, M. A. T., Hatziminaoglou, E., & da Costa, L. 2005, A&A, 436, 895
Gray, R. O., Corbally, C. J., Garrison, R. F., et al. 2006, AJ, 132, 161
Hadden, S. & Lithwick, Y. 2014, ApJ, 787, 80
Hansen, B. M. S. 2017, MNRAS, 467, 1531
Huang, C. X., Burt, J., Vanderburg, A., et al. 2018, ArXiv e-prints [arXiv:1809.05967]
Huang, C. X., Petrovich, C., & Deibert, E. 2017, AJ, 153, 210
Jones, H. R. A., Paul Butler, R., Tinney, C. G., et al. 2002, MNRAS, 333, 871
Kipping, D. M. 2010, MNRAS, 408, 1758
Kjeldsen, H. & Bedding, T. R. 1995, A&A, 293, 87
Kovács, G., Zucker, S., & Mazeh, T. 2002, A&A, 391, 369
Kubyshkina, D., Fossati, L., Erkaev, N. V., et al. 2018, ArXiv e-prints [arXiv:1809.06645]
Kurucz, R. L. 2013, ATLAS12: Opacity sampling model atmosphere program, Astrophysics Source Code Library
Lo Curto, G., Pepe, F., Avila, G., et al. 2015, The Messenger, 162, 9
Lopez, E. D. & Fortney, J. J. 2013, ApJ, 776, 2
Luri, X., Brown, A. G. A., Sarro, L. M., et al. 2018, ArXiv e-prints [arXiv:1804.09376]
Mandel, K. & Agol, E. 2002, ApJ, 580, L171
Mathur, S., García, R. A., Régulo, C., et al. 2010, A&A, 511, A46
Mayor, M., Pepe, F., Queloz, D., et al. 2003, The Messenger, 114, 20
Meadows, V. & Seager, S. 2010, Terrestrial Planet Atmospheres and Biosignatures, ed. S. Seager, 441–470
Mermilliod, J.-C. 1987, A&AS, 71, 413
Mustill, A. J., Davies, M. B., & Johansen, A. 2017, MNRAS, 468, 3000
Niraula, P., Redfield, S., Dai, F., et al. 2017, AJ, 154, 266
Öberg, K. I., Murray-Clay, R., & Bergin, E. A. 2011, ApJ, 743, L16
Owen, J. E. & Wu, Y. 2013, ApJ, 775, 105
Owen, T., Mahaffy, P., Niemann, H. B., et al. 1999, Nature, 402, 269
Pires, S., Mathur, S., García, R. A., et al. 2015, A&A, 574, A18
Piskunov, N. & Valenti, J. A. 2017, A&A, 597, A16
Ricker, G. R., Winn, J. N., Vanderspek, R., et al. 2015, Journal of Astronomical Telescopes, Instruments, and Systems, 1, 014003
Seager, S. & Deming, D. 2010, ARA&A, 48, 631
Silva Aguirre, V., Davies, G. R., Basu, S., et al. 2015, MNRAS, 452, 2127
Southworth, J., Wheatley, P. J., & Sams, G. 2007, MNRAS, 379, L11
Starck, J.-L. & Murtagh, F. 2002
Starck, J.-L. & Murtagh, F. 2006, Astronomical Image and Data Analysis
Valenti, J. A. & Fischer, D. A. 2005, ApJS, 159, 141
Valenti, J. A. & Piskunov, N. 1996, A&AS, 118, 595
Van Eylen, V., Agentoft, C., Lundkvist, M. S., et al. 2018a, MNRAS, 479, 4786
Van Eylen, V. & Albrecht, S. 2015, ApJ, 808, 126
Van Eylen, V., Albrecht, S., Huang, X., et al. 2018b, ArXiv e-prints [arXiv:1807.00549]
Weiss, A. & Schlattl, H. 2008, Ap&SS, 316, 99
Xie, J.-W., Dong, S., Zhu, Z., et al. 2016, Proceedings of the National Academy of Science, 113, 11431
Zechmeister, M. & Kürster, M. 2009, A&A, 496, 577
Zeng, L., Sasselov, D. D., & Jacobsen, S. B. 2016, ApJ, 819, 127

[1] Dipartimento di Fisica, Università degli Studi di Torino, via Pietro Giuria 1, I-10125, Torino, Italy
e-mail: `davide.gandolfi@unito.it`
[2] Department of Astronomy, Graduate School of Science, The University of Tokyo, Hongo 7-3-1, Bunkyo-ku, Tokyo, 113-0033, Japan
[3] Department of Space, Earth and Environment, Chalmers University of Technology, Onsala Space Observatory, 439 92 Onsala, Sweden
[4] Leiden Observatory, University of Leiden, PO Box 9513, 2300 RA, Leiden, The Netherlands
[5] Stellar Astrophysics Centre, Deparment of Physics and Astronomy, Aarhus University, Ny Munkegrade 120, DK-8000 Aarhus C, Denmark
[6] Astronomy Department and Van Vleck Observatory, Wesleyan University, Middletown, CT 06459, USA
[7] Space Research Institute, Austrian Academy ofSciences, Schmiedlstrasse 6, A-8041 Graz, Austria
[8] Departamento de Astrofísica, Universidad de La Laguna, E-38206, Tenerife, Spain
[9] Instituto de Astrofísica de Canarias, C/ Vía Láctea s/n, E-38205, La Laguna, Tenerife, Spain
[10] Rheinisches Institut für Umweltforschung, Abteilung Planetenforschung an der Universität zu Köln, Aachener Strasse 209, 50931 Köln, Germany
[11] Institute of Planetary Research, German Aerospace Center, Rutherfordstrasse 2, 12489 Berlin, Germany
[12] IRFU, CEA, Université Paris-Saclay, F-91191 Gif-sur-Yvette, France
[13] Université Paris Diderot, AIM, Sorbonne Paris Cité, CEA, CNRS, F-91191 Gif-sur-Yvette, France
[14] Department of Astrophysical Sciences, Princeton University, 4 Ivy Lane, Princeton, NJ, 08544, USA
[15] Thüringer Landessternwarte Tautenburg, Sternwarte 5, D-07778 Tautenberg, Germany
[16] Department of Astronomy and McDonald Observatory, University of Texas at Austin, 2515 Speedway, Stop C1400, Austin, TX 78712, USA

Table 2. π Men system parameters.

Parameter	Prior[(a)]	Final value
Stellar parameters		
Star mass $M_\star$ ($M_\odot$)	···	1.02 ± 0.03
Star radius $R_\star$ ($R_\odot$)	···	1.10 ± 0.01
Effective Temperature $T_{\rm eff}$ (K)	···	5870 ± 50
Surface gravity[(b)] $\log g_\star$ (cgs)		4.36 ± 0.02
Surface gravity[(c)] $\log g_\star$ (cgs)		4.33 ± 0.09
Iron abundance [Fe/H] (dex)		0.05 ± 0.09
Projected rotational velocity $v \sin i_\star$ (km s^{-1})		3.3 ± 0.5
Age (Gyr)		5.2 ± 1.1
Model parameters of π Men b		
Orbital period $P_{\rm orb}$ (days)	$\mathcal{U}[2079.5, 2109.5]$	2091.2 ± 2.0
Time of minimum conjunction T_0 (BJD$_{\rm TDB}$−2 450 000)	$\mathcal{U}[6531.9928, 6571.9928]$	8325.5011 ± 0.0017
$\sqrt{e} \sin \omega$	$\mathcal{U}[-1, 1]$	-0.3918 ± 0.0076
$\sqrt{e} \cos \omega$	$\mathcal{U}[-1, 1]$	0.6971 ± 0.0053
Radial velocity semi-amplitude variation K (m s^{-1})	$\mathcal{U}[0, 500]$	195.8 ± 1.5
Model parameters of π Men c		
Orbital period $P_{\rm orb}$ (days)	$\mathcal{U}[6.2416, 6.2916]$	6.26833 ± 0.00029
Transit epoch T_0 (BJD$_{\rm TDB}$−2 450 000)	$\mathcal{U}[8325.4787, 8325.5287]$	8325.5011 ± 0.0017
Scaled semi-major axis $a/R_\star$	$\mathcal{N}[12.3, 0.33]$	13.10 ± 0.17
Planet-to-star radius ratio $R_{\rm p}/R_\star$	$\mathcal{U}[0, 0.1]$	0.01532 ± 0.00041
Impact parameter, b	$\mathcal{U}[0, 1]$	$0.616^{+0.034}_{-0.035}$
$\sqrt{e} \sin \omega$	$\mathcal{F}[0]$	0
$\sqrt{e} \cos \omega$	$\mathcal{F}[0]$	0
Radial velocity semi-amplitude variation K (m s^{-1})	$\mathcal{U}[0, 10]$	1.54 ± 0.27
Additional model parameters		
Parameterized limb-darkening coefficient q_1	$\mathcal{N}[0.36, 0.1]$	0.35 ± 0.10
Parameterized limb-darkening coefficient q_2	$\mathcal{N}[0.25, 0.1]$	0.23 ± 0.10
Systemic velocity $\gamma_{\rm ATT}$ (km s^{-1})	$\mathcal{U}[-0.3036, 0.2951]$	0.0021 ± 0.0011
Systemic velocity $\gamma_{\rm HS1}$ (km s^{-1})	$\mathcal{U}[10.5307, 10.8832]$	10.70916 ± 0.00040
Systemic velocity $\gamma_{\rm HS2}$ (km s^{-1})	$\mathcal{U}[10.5611, 10.7750]$	10.73156 ± 0.00071
RV jitter term $\sigma_{\rm ATT}$ (m s^{-1})	$\mathcal{U}[0, 100]$	$4.3^{+1.1}_{-1.0}$
RV jitter term $\sigma_{\rm HS1}$ (m s^{-1})	$\mathcal{U}[0, 100]$	$2.4^{+0.19}_{-0.17}$
RV jitter term $\sigma_{\rm HS2}$ (m s^{-1})	$\mathcal{U}[0, 100]$	$1.68^{+0.38}_{-0.29}$
Derived parameters of π Men b		
Planet minimum mass $M_{\rm p} \sin i$ ($M_{\rm J}$)	···	9.66 ± 0.20
Semi-major axis of the planetary orbit a (AU)	···	3.22 ± 0.05
Orbit eccentricity e	···	0.6394 ± 0.0025
Argument of periastron of stellar orbit $\omega_\star$ (degrees)	···	330.66 ± 0.65
Derived parameters of π Men c		
Planet mass $M_{\rm p}$ ($M_\oplus$)	···	4.51 ± 0.81
Planet radius $R_{\rm p}$ ($R_\oplus$)	···	$1.838^{+0.053}_{-0.052}$
Planet mean density $\rho_{\rm p}$ (g cm^{-3})	···	$3.99^{+0.81}_{-0.77}$
Semi-major axis of the planetary orbit a (AU)	···	0.0670 ± 0.0011
Orbit eccentricity e	···	0 (fixed)
Orbit inclination $i_{\rm p}$ (degrees)	···	87.30 ± 0.17
Transit duration τ_{14} (hours)	···	$2.96^{+0.08}_{-0.09}$
Equilibrium temperature[(d)] $T_{\rm eq}$ (K)	···	1147 ± 12

Note – [(a)] $\mathcal{U}[a, b]$ refers to uniform priors between a and b, and $\mathcal{F}[a]$ to a fixed a value. [(b)] From spectroscopy and isochrones. [(c)] From spectroscopy. [(d)] Assuming albedo = 0.

Table 3. UCLES RV measurements of π Men.

BJD^{a}_{TDB} -2450000	RV ($km\,s^{-1}$)	$\pm\sigma$ ($km\,s^{-1}$)
829.993723	-0.0410	0.0048
1119.251098	-0.0674	0.0098
1236.033635	-0.0792	0.0060
1411.325662	-0.0858	0.0058
1473.267712	-0.0800	0.0048
1526.081162	-0.0930	0.0046
1527.082805	-0.0898	0.0041
1530.128708	-0.0879	0.0045
1629.912366	-0.0927	0.0056
1683.842991	-0.1005	0.0050
1828.188260	-0.0674	0.0048
1919.099660	-0.0350	0.0072
1921.139081	-0.0373	0.0047
1983.919846	-0.0028	0.0056
2060.840355	0.1361	0.0048
2092.337359	0.2120	0.0047
2093.352231	0.2094	0.0044
2127.328562	0.2878	0.0059
2128.336410	0.2861	0.0042
2130.339049	0.2899	0.0067
2151.292440	0.3079	0.0052
2154.305009	0.3030	0.0100
2187.196618	0.2857	0.0039
2188.236606	0.2893	0.0037
2189.223031	0.2797	0.0033
2190.145881	0.2835	0.0037
2387.871387	0.1009	0.0036
2389.852023	0.0974	0.0033
2510.307394	0.0417	0.0042
2592.126975	0.0202	0.0032
2599.155380	0.0210	0.0120
2654.099326	0.0188	0.0047
2751.918480	-0.0117	0.0042
2944.224628	-0.0434	0.0038
3004.075458	-0.0321	0.0044
3042.078745	-0.0440	0.0042
3043.018085	-0.0463	0.0045
3047.050110	-0.0408	0.0043
3048.097508	-0.0444	0.0036
3245.311649	-0.0697	0.0050
3402.035747	-0.0669	0.0018
3669.244092	-0.0863	0.0019

Notes:
[a] Barycentric Julian dates are given in barycentric dynamical time.

Table 4. HARPS RV measurements of π Men acquired with the old fibre bundle. The entire RV data set is available in a machine-readable table in the on-line journal.

BJD^{a}_{TDB} -2450000	RV ($km\,s^{-1}$)	$\pm\sigma$ ($km\,s^{-1}$)	BIS ($km\,s^{-1}$)	FWHM ($km\,s^{-1}$)	T_{exp} (s)	S/N [b]
3001.830364	10.6600	0.0014	-0.0019	7.6406	109	69.0
3034.607261	10.6665	0.0008	0.0040	7.6368	200	120.7
3289.869718	10.6448	0.0012	-0.0013	7.6378	60	79.6
3289.870782	10.6428	0.0011	-0.0012	7.6406	60	89.4
3289.871836	10.6446	0.0011	-0.0007	7.6394	60	90.7
3289.872866	10.6449	0.0011	-0.0026	7.6439	60	86.5
...	...	...	...	...	...	...

Notes:
[a] Barycentric Julian dates are given in barycentric dynamical time.
[b] S/N per pixel at 550 nm.

Table 5. HARPS RV measurements of π Men acquired with the new fibre bundle.

BJD^{a}_{TDB} -2450000	RV ($km\,s^{-1}$)	$\pm\sigma$ ($km\,s^{-1}$)	BIS ($km\,s^{-1}$)	FWHM ($km\,s^{-1}$)	T_{exp} (s)	S/N [b]
7298.853243	10.6750	0.0005	0.0081	7.6856	450	187.3
7298.858243	10.6747	0.0004	0.0083	7.6842	450	242.8
7327.755817	10.6744	0.0003	0.0089	7.6870	900	305.7
7354.783687	10.6674	0.0002	0.0104	7.6867	900	538.0
7357.725912	10.6727	0.0002	0.0105	7.6858	900	542.9
7372.705131	10.6664	0.0004	0.0094	7.6825	300	273.0
7372.708997	10.6662	0.0004	0.0118	7.6822	300	247.3
7372.712758	10.6654	0.0003	0.0104	7.6831	300	320.9
7423.591772	10.6630	0.0005	0.0113	7.6796	450	217.1
7423.597918	10.6628	0.0005	0.0115	7.6782	450	214.1
7424.586637	10.6645	0.0004	0.0104	7.6814	450	299.7
7424.592367	10.6643	0.0004	0.0113	7.6816	450	288.5
7462.517924	10.6612	0.0003	0.0116	7.6822	450	326.8
7462.523491	10.6612	0.0003	0.0106	7.6816	450	337.8
7464.499915	10.6616	0.0005	0.0083	7.6812	300	217.7
7464.503781	10.6627	0.0004	0.0112	7.6818	300	276.2
7464.507474	10.6611	0.0004	0.0108	7.6820	300	286.4

Notes:
[a] Barycentric Julian dates are given in barycentric dynamical time.
[b] S/N per pixel at 550 nm.